A comparative study of atmospheric and laboratory-analogue numerical tornado-vortex models

By PETER A. C. HOWELLS[1], RICHARD ROTUNNO

National Center for Atmospheric Research[2], Boulder, CO., 80307

and

ROGER K. SMITH

Department of Mathematics, Monash University, Clayton, Victoria, Australia, 3168

SUMMARY

A detailed sensitivity study of a tornado-vortex model developed by Howells and Smith is presented in order to draw a comparison between the results of various axisymmetric models that purport to simulate laboratory and tornadic vortices. The model incorporates a stretched finite-difference mesh in both radial and vertical directions and this provides for an increase in resolution in the vicinity of the vortex core and lower-boundary layer. The development of the vortex is studied for different values of two key parameters. These are the ratio of the applied tangential velocity to the mean vertical velocity (the swirl ratio) and the Reynolds' number based on the eddy diffusivity coefficient, the mean radial velocity, and the radius of the domain. Most of the simulations are for a no-slip lower boundary, but a few free-slip experiments are presented for comparison. These serve to highlight the importance of the radial inflow jet for the no-slip case.

Emphasis is placed in the no-slip experiment on the relative importance of the primary meridional circulation associated directly with the applied forcing, and the secondary circulation induced by the lower-boundary layer. For weak applied swirl (tangential) velocity ($1 \, \mathrm{m \, s^{-1}}$), the secondary circulation is relatively weak and the maximum tangential velocity is associated with the convergence produced by the primary circulation. Accordingly, this maximum occurs at a substantial height above the lower boundary. For moderate applied swirl velocity ($4 \, \mathrm{m \, s^{-1}}$), the secondary circulation is manifest as a strong radial inflow jet near the lower boundary. This jet advects rotating air close to the axis. The flow that evolves is dependent on the magnitude of the eddy turbulent diffusivity coefficient. For a relatively low diffusivity coefficient ($10 \, \mathrm{m^2 s^{-1}}$), a large amplitude centrifugal wave forms and breaks violently near the corner region. At higher values ($20 \, \mathrm{m^2 s^{-1}}$), a quasi-steady toroidal vortex develops in the region where the stream surfaces expand, and the maximum swirl velocity is found to occur at low levels near the corner region. This breakdown feature is advected out of the domain when the diffusivity coefficient is increased to $30 \, \mathrm{m^2 s^{-1}}$. When the simulations are performed using high imposed swirl velocities ($10 \, \mathrm{m \, s^{-1}}$), a very intense vortex forms with maximum tangential velocity exceeding $55 \, \mathrm{m \, s^{-1}}$, despite the frictional losses near the ground. This is considerably stronger than the equivalent free-slip vortex which attains a maximum tangential velocity of $44 \, \mathrm{m \, s^{-1}}$. Although many of these results have been obtained in past numerical studies, a clear demonstration of the importance of the secondary circulation as compared with the primary circulation has not been forthcoming due to a wide variety of experimental configurations and external parameters.

1. INTRODUCTION

The basis for all numerical simulations of tornado-like vortices is that an updraught, when imposed on a swirling flow, will lead to a local intensification of the swirl (tangential) velocity as angular-momentum-conserving fluid parcels are drawn in towards the centre of the updraught. The apparent simplicity of this idea is complicated because the swirling flow, through its interaction with the lower boundary, develops a secondary circulation which may locally supersede the original imposed updraught. In this paper we examine the relative importance of the primary versus the secondary circulations using the axisymmetric vortex model described by Howells and Smith (1983).

The secondary circulation results from the application of the no-slip lower boundary condition, which according to boundary-layer theory, reduces the centrifugal acceleration per unit mass, but not the inward radial pressure force. This leads to an inward flow in the boundary layer which brings swirling air closer to the central axis than would have been possible without the boundary layer. Whether or not this leads to a more intense swirling flow depends, however, on the additional rate at which angular momentum is diffused to the surface. It is possible to envisage three extreme cases:

(i) Free-slip boundary: since there is no boundary layer there is only the primary circulation.

(ii) No-slip lower boundary, large diffusion: there is a secondary circulation and a less intense vortex than in (i) due to the relatively large frictional torque at the lower boundary.

(iii) No-slip lower boundary, small diffusion: there is an intense secondary circulation and a more intense vortex than in (i) due to additional boundary-layer convergence, the frictional torque being relatively small.

All of these features are included in past numerical simulations, but owing to the wide variety of experimental configurations, external parameters etc., a clear, unambiguous demonstration of the importance of the secondary circulation vis-à-vis the primary circulation in the tornado-vortex models has not been forthcoming. For example, numerical simulations by Harlow and Stein (1974) and Rotunno (1977) emphasized experiments using free-slip lower conditions. Thus they were concerned with the primary circulation as the one that directly creates the tornado vortex. Both these studies were based on Ward's laboratory vortex chamber (Ward 1972), the conception of which recognized that the width of the thunderstorm updraught is typically an order of magnitude larger than the tornado vortex itself. For medium to large values of the swirl ratio (ratio of imposed swirl velocity to imposed updraught) two-cell vortices were produced. Bode *et al.* (1975) and Smith and Leslie (1976), motivated by laboratory experiments of Turner (1966), explored the manner in which a concentrated axial body force imposed on a rotating flow will create a strong vortex. This method of forcing precluded the development of a two-celled vortex. However, whether or not a two-celled vortex is obtained is a minor issue. What is important is to recognize that all these studies emphasize the role of the primary circulation, the last two not through the choice of free-slip at the lower boundary, but by the choice of a relatively large diffusivity coefficient. The importance of the secondary circulation was not clear from these simulations; indeed, Bode *et al.* (1975) and Harlow and Stein (1974) found that application of a no-slip condition at the ground decreases the strength of the vortex, while Rotunno (1979) found the opposite. Lewellen and Teske (1977) report both effects depending on the surface roughness. Again owing to different driving mechanisms, effective Reynolds' numbers and swirl ratios, inter-model comparisons were not readily available.

The aim of the present study is to determine under what conditions each type of vortex emerges in a set of numerical experiments specifically designed for this purpose. For that reason, we use the axisymmetric numerical model of Howells and Smith (1983), in which a cloud-like forcing is imposed on a rotating flow, and adjust the numerical values of the nondimensional parameters so that they nearly match those of the laboratory vortex chamber. Through systematic variations we then can determine precisely which vortex exists in a given regime, and whether or not the cloud-like model is in any significant way different from the laboratory model. Particular interest is focused on case (iii) above, where the demands of the frictional constraint in the radial and azimuthal directions are rather subtle.

As in the laboratory models, vortex structure is found to be sensitive to two key fluid-dynamical parameters; namely, the imposed swirl velocity at the radial boundary and the magnitude of the eddy diffusivity coefficient. Both quantities are assumed to be constant in this study. The two parameters can be represented in terms of the non-dimensional swirl ratio and the radial Reynolds' number respectively. The swirl ratio is defined as $S = V/\bar{w}$, and is simply the ratio of the imposed tangential velocity at the radial boundary, V, to the average vertical velocity through the top of the domain. The nomenclature, which is more or less standard, is given in appendix A. In the calculations presented in this paper, the swirl ratio varies from 0·2 to 2·0. The radial Reynolds' number is defined as $R_e = UR/K$, where U is the radial velocity at a distance R from the axis (usually taken to be the position of the lateral boundary), and K is the eddy diffusivity coefficient. The radial Reynolds' number in this study varies between 100 and 1000.

Results from the present study indicate that vortex breakdown occurs when approximately $R_e > 1000$ and $S > 0·2$ and there is no slip at the lower boundary as in the laboratory model. However, unlike the laboratory situation, vortex breakdown can be more easily controlled in the numerical model by substantially reducing the Reynolds' number. It is shown herein that vortex breakdown involves a complex interaction between two competing tendencies. The first, a manifestation of the no-slip condition, favours the production of an axial updraught as an extension of the convergent boundary layer, but leads to a low-level tangential wind maximum due to the strong inward advection of swirling air. The second is associated with the decay of the tangential velocity with height, and hence, to an adverse axial pressure gradient (cf. Smith and Howells (1983), especially p. 293). This pressure gradient tends to oppose this axial upflow and may even reverse it. In turn, the retardation of the axial flow must be accompanied by radial outflow. This represents the breakdown of the vortex. In the most severe case of breakdown, a large amplitude centrifugal wave forms, breaks violently and triggers a series of waves along the entire vertical axis. With weaker applied swirl velocity or higher diffusion, a toroidal ring vortex forms at low levels and propagates along the axis. For still weaker swirl velocity or higher diffusivity coefficient, the expansion of the stream surfaces is only slight and is followed by a contraction as the flow undergoes cyclostrophic adjustment. The previous no-slip simulations by Howells and Smith were in this category. The above behaviour has many similarities with the transition from a laminar to a turbulent vortex as revealed by laboratory simulations (e.g. see Church *et al.* (1979), Fig. 5). Features which appear to be in common are a sudden expansion of the laminar vortex and a toroidal ring vortex near the crest of the leading centrifugal wave. Some wave-like structure is also evident above the breakdown.

2. MODEL FORMULATION

Details of the axisymmetric vortex model are given in Howells and Smith (1983). The calculations are performed in a cylindrical region of air of radius R, depth H, and with its axis vertical. The lower boundary is at the ground and air may enter or leave the domain in a normal direction through the upper and lateral boundaries. The flow is considered to be axisymmetric and rotation is imposed by prescribing a tangential velocity component on air entering through the lateral boundary. The equations used are similar to those derived by Ogura and Phillips (1962) for deep convection except that a non-adiabatic base state is incorporated. A summary of the equations and boundary conditions is given in appendix B. Several minor but important modifications have been made and are worth noting.

The number of grid points has been increased to 61 in the vertical direction and 41 in the radial direction. In order to resolve the important features of the flow while keeping computing time to a minimum, it was necessary to introduce a coordinate transformation (see e.g. Anthes 1970). The calculations were still very costly, taking up to 30 minutes of processing time on a CRAY 1A computer. The equations have been transformed in both the radial and vertical directions according to the following functions

$$r = R \sinh(\alpha x/R)/\sinh \alpha, \qquad x = R(i-1)/60, \quad i = 1, 2, 3, \ldots, 61$$

$$z = H \sinh(\beta y/H)/\sinh \beta, \qquad y = H(j-1)/40, \quad j = 1, 2, 3, \ldots, 41$$

where $R = 2000$ m and $H = 3000$ m. Note that x and y are the new independent variables. The parameters α and β define the degree of grid stretching and for most of the experiments conducted are both assigned the value 2·55. This gives a fairly uniform resolution of 20 m near the axis and lower boundary. The grid separation near the top and lateral boundaries is about 125 m. The mesh size is defined in this manner so as to give maximum resolution in the vortex core and boundary layer. Using the degree of stretching indicated above gives, at most, a 5% mesh expansion thus avoiding the possibility of troublesome internal grid reflection. Transforming the equations necessitates a change in the Poisson solver due to the variation of coefficients in the radial and vertical directions. The NCAR routine BLKTRI was used to perform this operation. Another small change made was that all second-order derivative terms were transformed into finite-difference form by applying the transformation for the first-order derivative successively.

As in Howells and Smith (1983), the effects of buoyancy due to latent heat release are represented by a broad body force in the vertical momentum equation. It has the form

$$F(r, z) = g(\Delta\theta/\theta_a) R(r) Z(z)$$

$$R(r) = \begin{cases} 1 - (r/r_1)^2 & 0 \leqslant r \leqslant r_1 \\ 0 & \text{otherwise} \end{cases}$$

$$Z(z) = \begin{cases} 0 & 0 \leqslant z \leqslant z_1 \\ 2(z - z_1) & z_1 < z \leqslant z_2 \\ 1 & \text{otherwise} \end{cases}$$

where g is the acceleration due to gravity, $\Delta\theta$ is a constant excess temperature deviation of 5 K, and θ_a is the ambient potential temperature defined as

$$\theta_a(z) = \begin{cases} 300 & z \leqslant z_2 \\ 300 + 2(z - z_2) & z > z_2 \end{cases}$$

where $r_1 = 1\cdot5$ km, $z_1 = 1\cdot0$ km and $z_2 = 1\cdot5$ km. Thus F has a maximum value equivalent to a buoyancy force with temperature excess 5 K (the mean excess is 2·2 K distributed over the forcing region). The body force is zero below 1 km, increases linearly with height to 1·5 km and is constant above this level. In the radial direction, the forcing decreases quadratically to zero at 1·5 km.

Due to the rapidly changing flow patterns associated with breakdown features, it was necessry to check the CFL linear advection criterion at every time step. The time step was set equal to

$$\Delta t = 0\cdot6 \min \left(\frac{\partial x}{\partial r} \frac{u}{\Delta x} + \frac{\partial y}{\partial z} \frac{w}{\Delta y} \right)^{-1},$$

that is, 60% of the CFL limit. For the free-slip experiment, the more stringent value of 40% was required in order to maintain computational stability.

The method for calculating the pressure field requires some explanation. The field was obtained by integrating the radial momentum equation outwards from the first interior mesh point near the base of the axis and then using the pressure values obtained to integrate explicitly the vertical momentum equation upwards. The field was then shifted so as to give a zero perturbation pressure at the first interior point near the top right-hand corner of the computational domain. A few forward time steps were performed due to problems associated with the adoption of the second-order Miller–Pearce time extrapolation procedure. The pressure field obtained was found to be far more accurate than the method outlined in Howells and Smith (1983).

Finally, a comment on the use of a constant eddy diffusivity coefficient. Very little is known about the role of turbulence in rapidly rotating flows. The turbulence produced by shear instabilities must be suppressed to some extent in the centrifugally stable vortex core. Indeed, many observations of tornadoes and waterspouts reveal a core with a remarkably laminar appearance. A turbulence parametrization based on local properties of the flow (like the deformation rate) would require some modification due to the stabilizing effects of not only stratification but also rotation. Lewellen and Sheng (1980) used a second-order closure scheme in their simulation of a tornado-like vortex. In order to make comparisons with other model results and laboratory vortices we adopt the simple parameter approach. Note also that isotropic turbulence is assumed so that the eddy coefficients are the same in both the radial and vertical directions. The more unconventional split form was adopted by Howells and Smith (1983). In this present work, the value of the eddy coefficient was always larger than that required to prevent computational instabilities from arising due to large unresolvable gradients in the vortex core and boundary layer. Indeed, for a given set of experimental parameters, the smallest value of the diffusivity parameter used was marginally larger than that required for numerical stability.

3. RESULTS OF THE NUMERICAL CALCULATIONS

(a) No-swirl experiment (S = 0)

Figure 1 shows steady-state meridional cross-sections of streamfunction, radial and vertical velocity for no imposed swirl velocity at the lateral boundary and a diffusivity coefficient[1] of $20 \, \text{m}^2\text{s}^{-1}$. Many previous studies of this type of flow show the boundary layer separating off the lower surface (see e.g. Rotunno (1979), Fig. 4.1). It is clear from Fig. 2 that the present experimental configuration leads to the development of a pressure distribution conducive to inflow near the entire lower surface, unlike the numerical experiments of Ward (1972) and Rotunno (1979).

In the latter, Rotunno argues that separation occurs in his experiments due to the increase in pressure towards the axis by considering the balance

$$-c_p \frac{\partial}{\partial r}(\theta_a \pi') = \frac{\partial}{\partial r}\left(\frac{u^2}{2}\right).$$
(3.1)

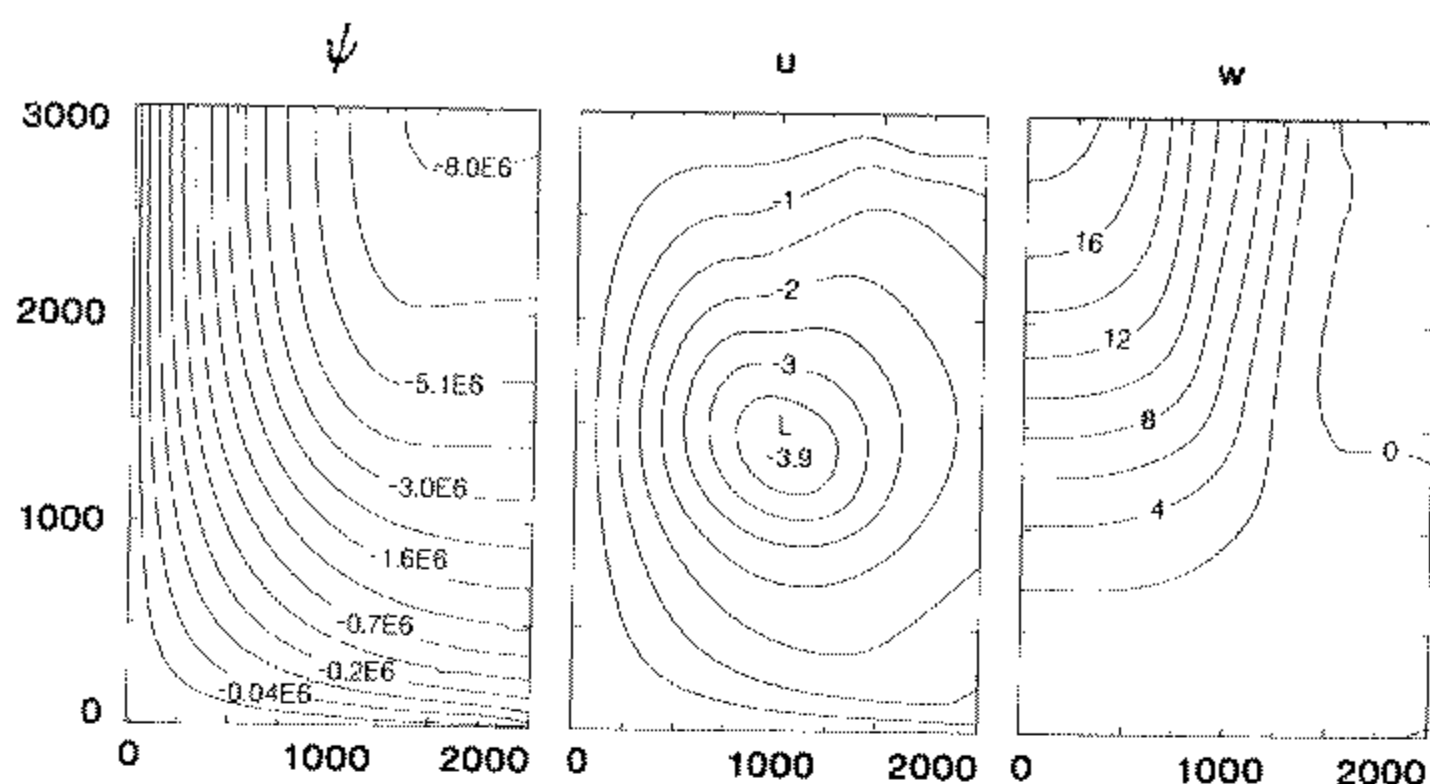[1] A smaller diffusivity could have been used but the results are fairly insensitive to its precise value.

Figure 1. Steady-state streamfunction, radial and axial velocities for $K = 20$ m²s⁻¹ and no imposed swirl velocity. The contour levels for the streamfunction have non-uniform spacings as indicated.
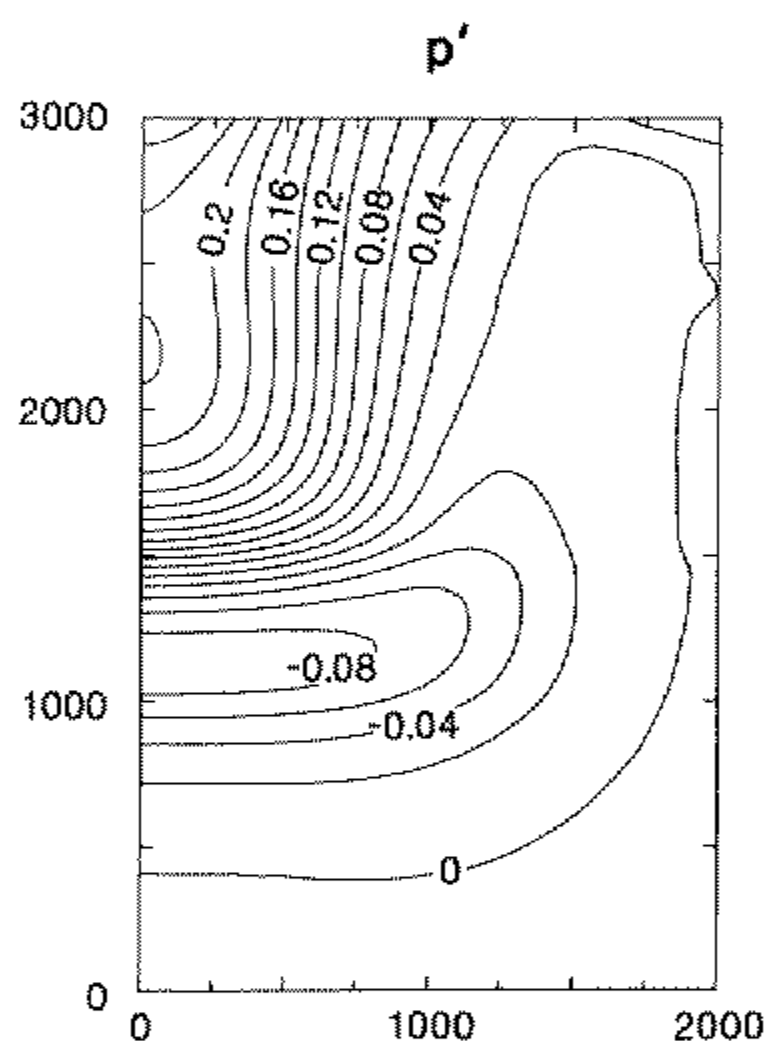
Figure 2. Steady-state perturbation pressure field for $K = 20$ m²s⁻¹ and no imposed swirl velocity. Contour labels are in mb.

However, in the present case, the vertical advection of radial momentum is important and the force balance is

$$-c_p \frac{\partial}{\partial r}(\theta_a \pi') = \frac{\partial}{\partial r}\left(\frac{u^2}{2}\right) + w\frac{\partial u}{\partial z}. \tag{3.2}$$

Figure 3 shows the radial force balance at a height of 1 km. The last term on the right-hand side of Eq. (3.2) is clearly comparable to the preceding term and cannot be neglected. The term contributes to the lowering of pressure beneath the forcing and hence to radial inflow.

In other experiments that were conducted, it was found that the boundary layer separates immediately after the applied forcing is switched off. Clearly, without the body force the pressure distribution becomes unfavourable to radial inflow along the entire lower boundary. In another experiment, flow separation occurred when the forcing was
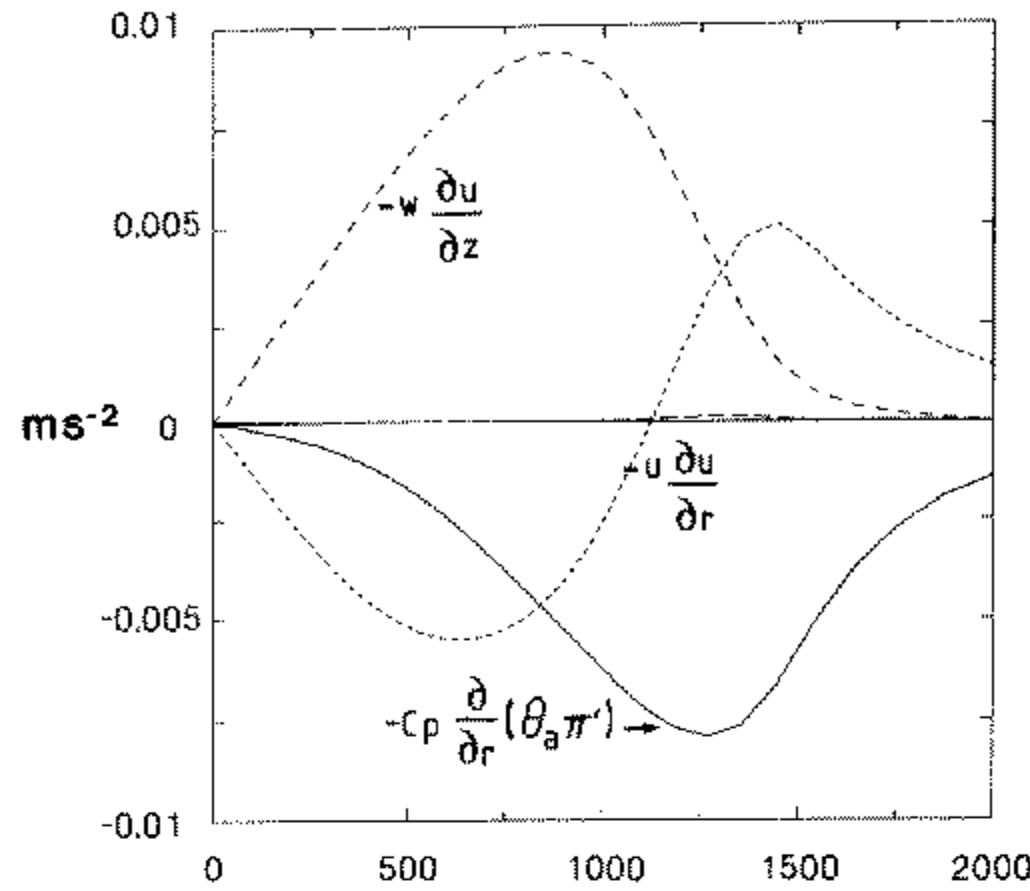
Figure 3. Steady-state distribution of radial forcing terms at a height of 1 km for the case $K = 20\,\mathrm{m^2 s^{-1}}$ and no imposed swirl.
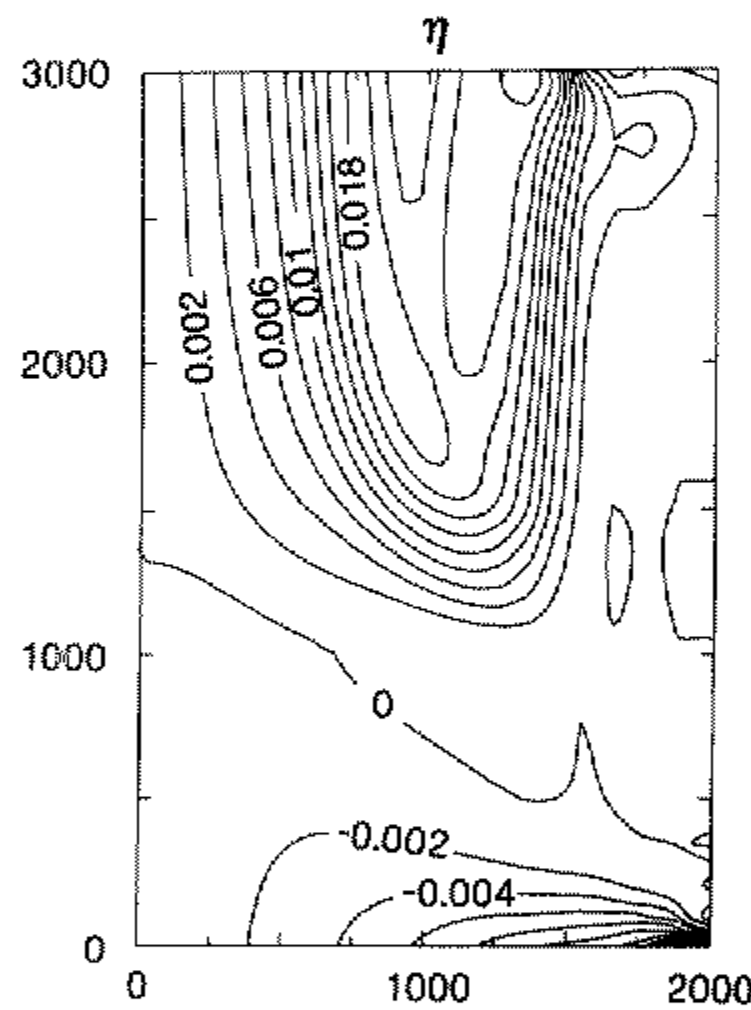

Figure 4. Steady-state meridional cross-section of azimuthal vorticity for the case $K = 20\,\mathrm{m^2 s^{-1}}$ and no imposed swirl velocity.

restricted to a very shallow region near the top of the domain. This configuration closely resembles the laboratory experiments and numerical calculations of Rotunno (1979). However, whether or not separation actually occurs is a minor issue in what follows. Wilson and Rotunno (1986, hereafter referred to as WR) show that, for the flow outside the boundary layer and core, there is good agreement between potential-flow solutions and the flow in the Purdue University laboratory vortex chamber. Figure 4 shows a meridional cross-section of azimuthal vorticity after 60 minutes. The positive vorticity at the top of the domain is due largely to the applied forcing, whereas negative vorticity near the ground has been generated at the no-slip lower boundary. Potential flow solutions can be calculated in a small region between the boundary layer and a height of about 1300 m corresponding to approximately irrotational flow and the lower convergence region studied by WR.

(b)   Experiments with free-slip

Figure 5 shows some steady-state results of a simulation using free-slip (i.e. zero stress) conditions at the lower boundary for various values of applied swirl velocities and eddy coefficients as indicated. As described above, the free-slip condition precludes the development of a surface boundary layer and is often associated with a two-cell vortex structure. This type of vortex has a steady-state maximum tangential velocity beneath the region of forcing. Above this position, there is an adverse axial pressure gradient associated with steady axial downflow in the core (cf. Eq. (3.3) below). During vortex development, the decay of swirl velocity with height can be attributed to turbulent diffusion; the adverse axial pressure gradient associated with this decay causes the axial flow to decelerate with a corrresponding radial divergence occurring near the axis. Evidence of this behaviour can be seen in Figs. 5(a) and (b). At a low swirl velocity of $V = 1 \text{ m s}^{-1}$ and diffusivity coefficient of $K = 4 \text{ m}^2\text{s}^{-1}$ (fields not shown), a relatively intense steady-state vortex forms with a maximum tangential velocity of $22 \cdot 7 \text{ m s}^{-1}$. In this case a transient downdraught occurs at 18 minutes with an intensity of 25 m s^{-1}. The downdraught lasts only a few minutes, however, and in the steady state there is upflow everywhere along the axis, albeit considerably retarded compared with the maximum upflow which occurs off the axis.
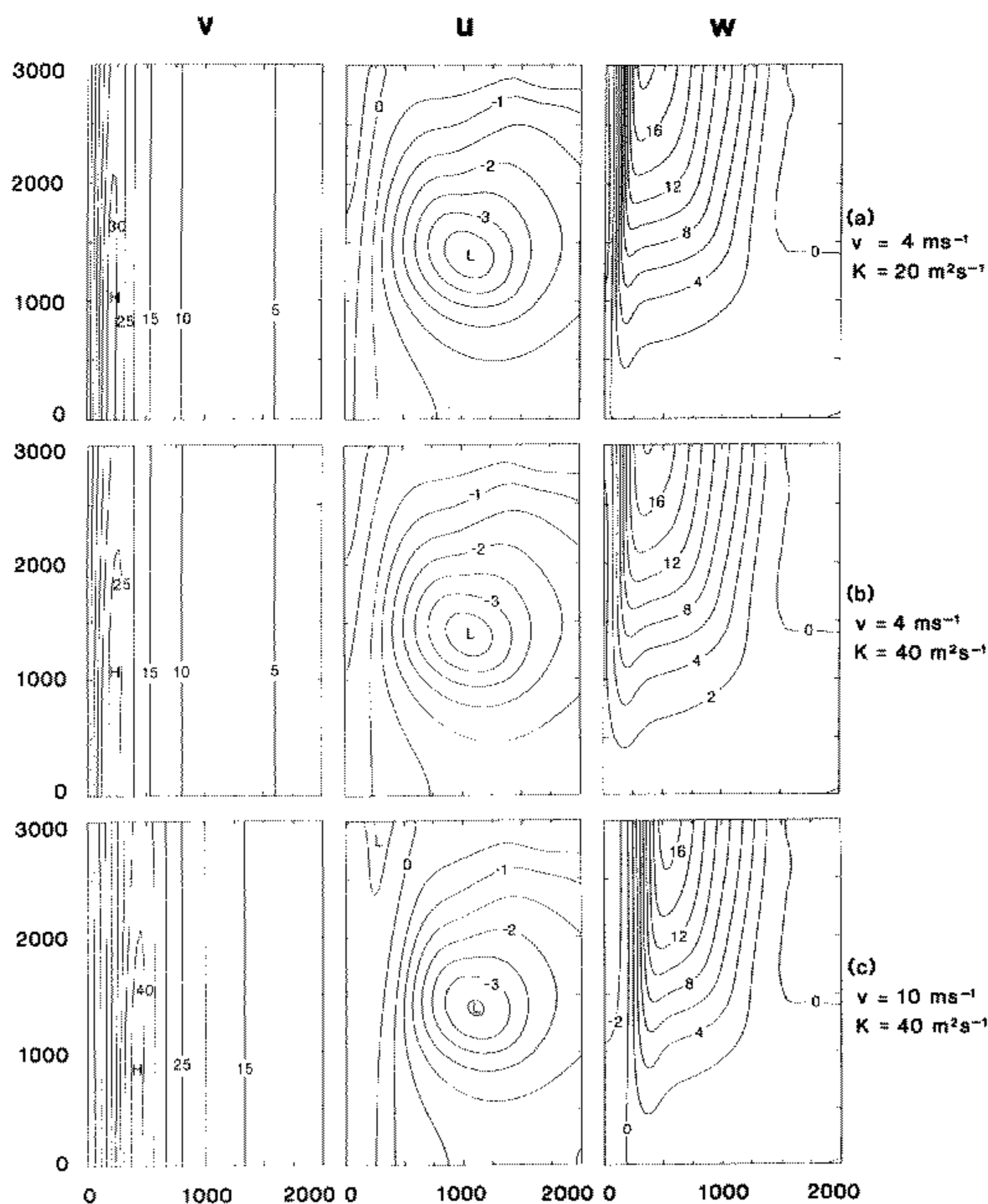

Figure 5.   Steady-state meridional cross-sections of tangential, radial and vertical velocity components for a free-slip lower boundary using various applied swirl velocities and diffusivities as indicated.

For the moderate swirl velocity of $4\,\mathrm{m\,s^{-1}}$ and a diffusivity coefficient of $20\,\mathrm{m^2 s^{-1}}$, a two-cell vortex develops with a steady downflow of about $2\,\mathrm{m\,s^{-1}}$ within the vortex core (see Fig. 5(a)). However, if the diffusivity coefficient is increased to $40\,\mathrm{m^2 s^{-1}}$ (Fig. 5(b)), the downflow is completely eliminated due to the increased mixing of vertical momentum across the core. The speed of the upflow is about $2\,\mathrm{m\,s^{-1}}$ and the maximum swirl velocity is reduced from $31\cdot4\,\mathrm{m\,s^{-1}}$ to $26\cdot4\,\mathrm{m\,s^{-1}}$.

At the higher applied swirl velocity of $10\,\mathrm{m\,s^{-1}}$, the two-cell structure is again achieved (Fig. 5(c)). The vortex is considerably wider, however, with a core diameter of $0\cdot5\,\mathrm{km}$ compared with $0\cdot25\,\mathrm{km}$ in Fig. 5(b). The vortex is broader because the applied forcing is unable to concentrate the higher angular momentum fluid to the same extent; a result consistent with laboratory studies and other numerical simulations. As noted above, the axial downflow is a consequence of an adverse pressure gradient which is strong enough to overcome the applied body force. As noted above, the axial pressure is intimately related to the swirling velocity field through the cyclostrophic balance (Smith and Howells 1983). This may be expressed as

$$\left.\frac{\partial w}{\partial t}\right|_{r=0} = -c_p \frac{\partial}{\partial z}(\theta_a \pi')\Big|_{r=0} - \frac{\partial}{\partial z}\int_0^R \frac{V^2}{r}\,dr. \qquad (3.3)$$

The change in the position of the maximum tangential wind from upper to lower levels during vortex development is evidently sufficient to cause axial downflow through the downward pressure gradient defined by Eq. (3.3). In the less extreme cases noted above, a defect in the vertical velocity is achieved with a decrease in the intensity of the updraught in the vicinity of the axis. These results parallel the laboratory-based numerical simulations of Rotunno (1977) and others.

(c) Experiments with no-slip

Even with a no-slip lower boundary condition, the vortex still becomes concentrated aloft due to the primary circulation and there is a corresponding lowering of the axial pressure associated with the approximate cyclostrophic balance across the vortex. The pressure across the boundary layer does not change appreciably as the tangential velocity approaches zero near the surface so an inward pressure gradient results and causes the formation of a radial inflow jet close to the ground. This jet has the potential for transporting rotating fluid close to the axis and the tangential wind speed increases as a consequence of conservation of angular momentum. This results in the establishment of an adverse axial pressure gradient immediately above the level of maximum tangential wind. If the swirling winds are not too strong, upflow along the axis is retarded, but not reversed, so that the maximum updraught occurs off the axis. This transient feature is generally short-lived and a one-cell vortex is established with maximum vertical velocity at any level on the axis. The resulting flow is often termed an end-wall vortex, with the vertical jet in the core erupting from the lower surface as an extension of the swirling boundary layer.

With higher ambient swirl velocity or less diffusion, the adverse pressure gradient can cause enough deceleration of the flow to create an axial downdraught. The downflow occurs for the same reasons as in the free-slip experiment. As before, the region of axial deceleration is often accompanied by radial outflow. The ensuing flow may take on the pattern of stationary or travelling toroidal vortices or centrifugal waves with the possibility of catastrophic breakdown associated with the breaking of these waves.

At this point it is worth reviewing the stability criteria of cylindrical flows. A cylindrical flow with no axial motion (i.e. velocity $= \{0, v(r), 0\}$) is stable to axisymmetric perturbation if

$$\partial \Gamma^2 / \partial r > 0 \qquad (3.4)$$

Γ being the circulation. This is Rayleigh's circulation criterion (Rayleigh 1916). Effectively the same criterion applies to the stability with respect to two-dimensional non-axisymmetric disturbances in r and ϕ, or more specifically, $\partial \Gamma / \partial r > 0$ is required (Drazin and Reid 1982, p. 80). A more useful criterion in the present context concerns the stability of the cylindrical flow with axial shear (i.e. velocity $= \{0, v(r), w(r)\}$). This is stable to axisymmetric disturbances if

$$R_i \equiv \frac{1}{r^3} \frac{\partial \Gamma^2}{\partial r} \Big/ \left(\frac{\partial w}{\partial r}\right)^2 > \frac{1}{4} \qquad (3.5)$$

everywhere (Howard and Gupta 1962). This is simply the rotating analogue of the Richardson number criterion with notably the rotation frequency replacing the buoyancy frequency.

Some theories purporting to explain vortex breakdown are given by Gartshore (1962), Hall (1967, 1972), Benjamin (1962, 1967) and are reviewed in Rotunno (1979). Benjamin (1962) suggests a method for determining whether a flow is super-critical based on infinitesimal perturbations of the cylindrical flow $(0, v(r), w(r))$. In his numerical laboratory-vortex simulations, Rotunno (1979) verifies this method. In the present model, the vortex breakdown occurs first immediately above the inflow jet. This is due in part to the fact that the swirling velocity is imposed along the entire lateral boundary. Rotunno showed that when the swirl velocity is tapered to zero at the ground over several grid intervals, the breakdown occurs higher along the axis.

(i) *Experiments with weak imposed swirl velocity* $(S = 0 \cdot 2)$. Figure 6(a) shows the tangential, radial and vertical velocity at 35 minutes for the case $V = 1 \, \mathrm{m \, s^{-1}}$ and $K = 4 \, \mathrm{m^2 \, s^{-1}}$. It can be seen that the concentration of swirl velocity near the 500 m level is associated with a deceleration in the axial flow between 500 and 1000 m. The wave feature decays rapidly and by 60 minutes (Fig. 6(b)), a steady one-cell vortex has formed with air parcels accelerating along the axis except for a short interval near 700 m. The maximum swirl velocity occurs near the top of the domain and presumably the low-level radial jet is unable to transport angular momentum towards the axis without appreciable frictional loss. The increase in swirl velocity with height contributes to an upward pressure gradient according to Eq. (3.1).

Force balances for this case are presented in Fig. 7. At high levels (above 500 m), a close cyclostrophic balance exists across the vortex. This is clearly evident in Fig. 7(a) which shows the balance at 1 km. At a height of 100 m (Fig. 7(b)), the advection terms make a significant contribution to the overall balance. Near the ground the diffusion term becomes important and the centrifugal term is relatively small (Fig. 7(c)). There seems to be a close similarity in the structure of the flow to that obtained in WR's numerical study of a laboratory vortex. In that work, the outer flow (i.e. where Γ is constant) was found to be essentially irrotational and inviscid, and hence could be modelled using potential-flow theory. In the present case, the outer flow is rotational as the presence of the stratification and applied forcing are source terms in the prognostic equation for azimuthal vorticity. Their effects were clearly seen in the steady-state meridional cross-section of azimuthal vorticity for the no-swirl velocity (Fig. 4). However, the surface boundary layer closely resembles the two-tiered structure obtained in WR
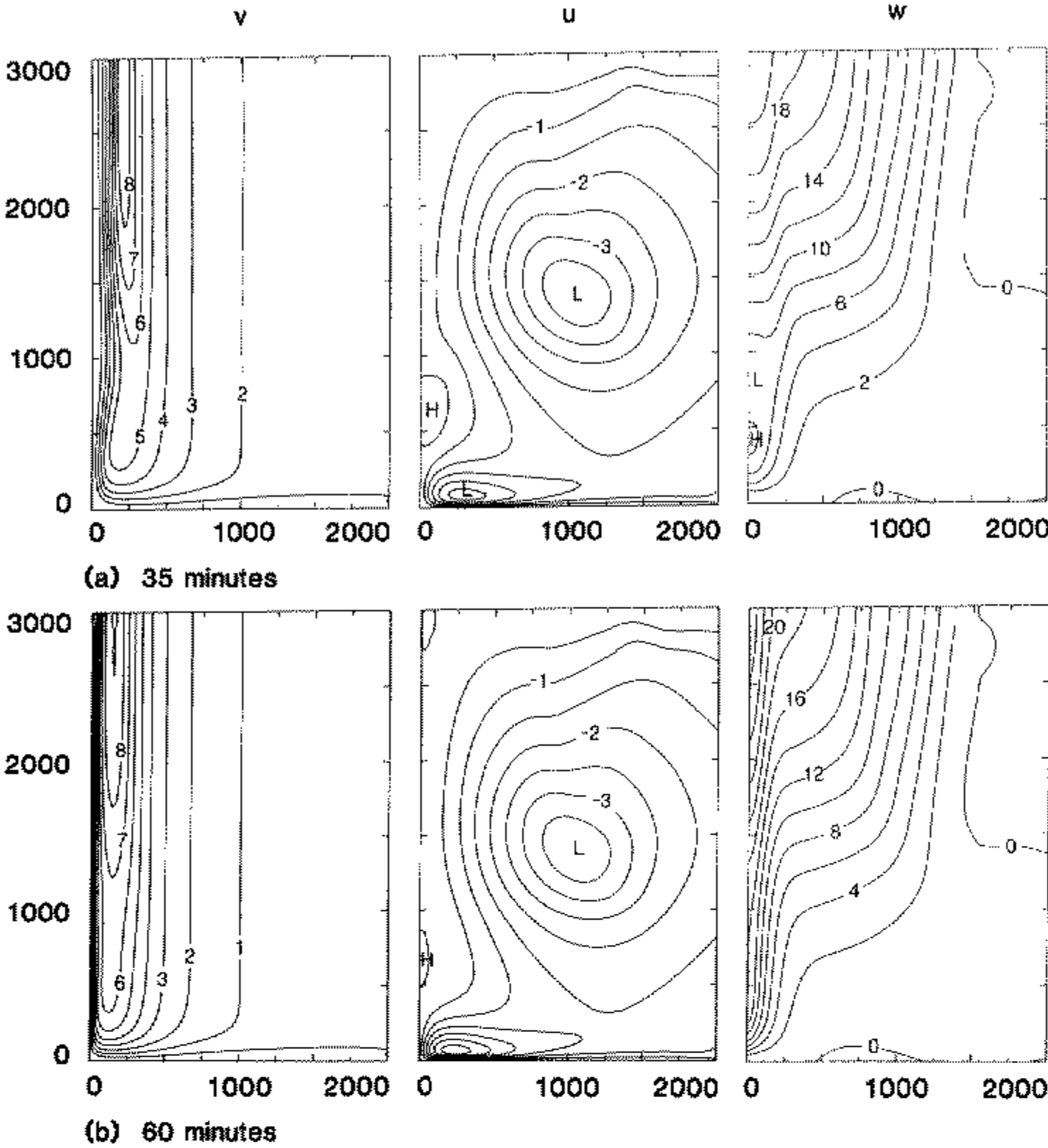
Figure 6. Meridional cross-sections of tangential, radial and vertical velocities for the case $V = 1\,\mathrm{m\,s^{-1}}$, $K = 4\,\mathrm{m^2\,s^{-1}}$ and a no-slip lower boundary at various times as indicated.
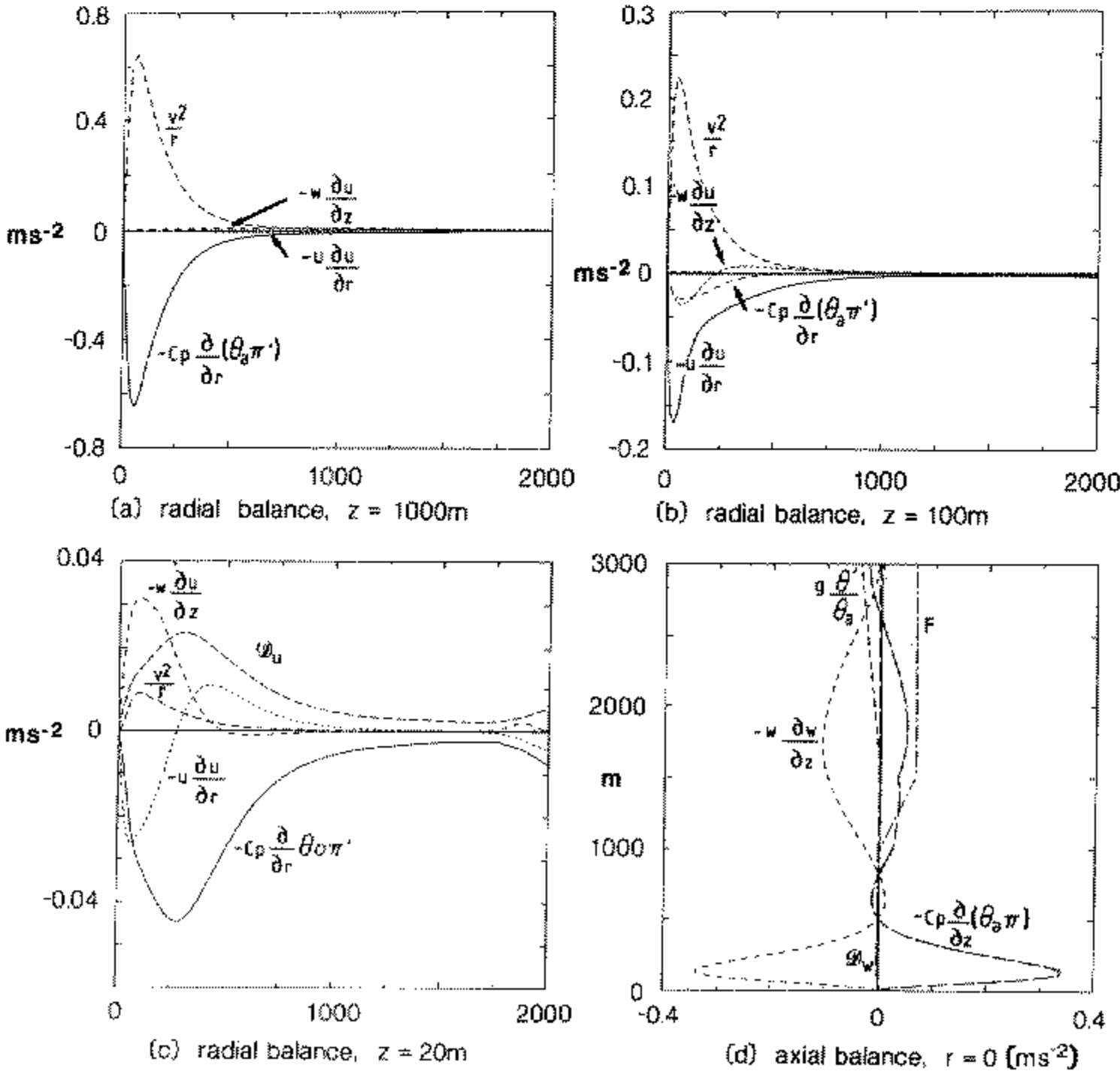

Figure 7. Steady-state distribution of force terms for the case of $V = 1\,\mathrm{m\,s^{-1}}$, $K = 4\,\mathrm{m^2s^{-1}}$ with (a), (b) and (c) representing the radial force balance at the 1 km, 100 m and 20 m levels respectively and (d), the axial distribution of vertical forcing terms.

and in earlier work by Burggraf *et al.* (1971) and Carrier (1971). WR found an outer layer which was laminar and rotational. This is consistent with the radial force balance in Fig. 7(b) where it is clear that the balance is principally between the inertial and pressure gradient terms. An inner sub-layer was found in WR in which the flow was rotational and viscous, and this appears to bear a close similarity to the boundary layer at 20 m (Fig. 7(c)). It should be recalled that WR employ molecular diffusion while the friction term in the present study is an attempt to incorporate the effects of turbulent eddies which would inevitably form in the shear layer near the ground. As in WR, the vortex core also exhibits a two-layer structure with the flow being mostly rotational and inviscid except for a small sub-core where viscous forces play some role. From Fig. 7(d) we can see that this term is small compared with others in the overall balance.

If the experiment is repeated with higher values of the diffusivity parameter the pattern remains similar except that the boundary layer, and correspondingly the vortex core, are broader and less intense, similar to the results of Harlow and Stein (1974). The present experiment is rather sensitive to the actual value of the diffusivity coefficient, which, if reduced, allows strong shear near the surface which cannot be resolved by the present grid.

(ii) *Experiments with moderate imposed swirl velocity* ($S = 1\cdot0$). Figure 8(a) shows the tangential, radial and vertical velocity at 18 minutes for the case $V = 4\,\mathrm{m\,s^{-1}}$ and $K = 10\,\mathrm{m^2s^{-1}}$. A strong jet has formed with a speed of about $10\,\mathrm{m\,s^{-1}}$. There is a corresponding maximum in the tangential velocity with a value of $15\,\mathrm{m\,s^{-1}}$ at a distance of 500 m from the axis. The vertical velocity pattern shows upflow at the head of the inflow jet. The outflow at 500 m is associated with a local minimum in the pressure field at the head of the jet (the perturbation pressure field for the lower-left quadrant of the domain is shown in Fig. 9(a)). Another interpretation of this phenomenon is that the inflow jet develops inertial overshoot so that centrifugal and radial pressure gradient terms are out of balance. Hence, there is a tendency for air parcels to flow outwards on exiting the inflow jet. A small region of axial downflow occurs soon after, with a speed of about $2\,\mathrm{m\,s^{-1}}$ but is a transient feature.

Figure 8(b) shows the velocity components contoured in the lower-left quadrant of the domain at 21 minutes. The inflow jet is more intense with a maximum of $12\,\mathrm{m\,s^{-1}}$ located about 300 m from the axis. The region of low pressure that first developed at the head of the inflow jet has merged with the axis (Fig. 9(b)). The flow accelerates rapidly up the axis and reaches a peak vertical velocity of $20\,\mathrm{m\,s^{-1}}$ at a height of 120 m corresponding to the level where the tangential wind is a maximum. The air parcels subsequently decelerate and move away from the axis due to inertial overshooting of the inflow jet. The axial updraught is reduced to $0\cdot8\,\mathrm{m\,s^{-1}}$ at the 300 m level. The outflow region, to a good approximation, mirrors the inflow jet, but decelerates rapidly however, and turns back towards the axis at a radius of 300 m. This is caused by the flow inertially undershooting its equilibrium position. A close cyclostrophic balance exists across the vortex core above 700 m. A secondary maximum in the tangential wind at 700 m produces a lowering of pressure near the axis and this is responsible for the strong axial upflow between the 300 and 700 m levels. Situated between this upflow and the one located 300 m from the axis is a region of subsidence. This downflow is formed as air is extracted above 250 m by the axial updraught and leads to the downward transport of angular momentum (Fig. 9(c)). The fold in the angular momentum surface is an unstable configuration as a consequence of the Rayleigh circulation theorem (Eq. (3.4)). The wave breaks violently and the ensuing flow is extremely turbulent. The present model is
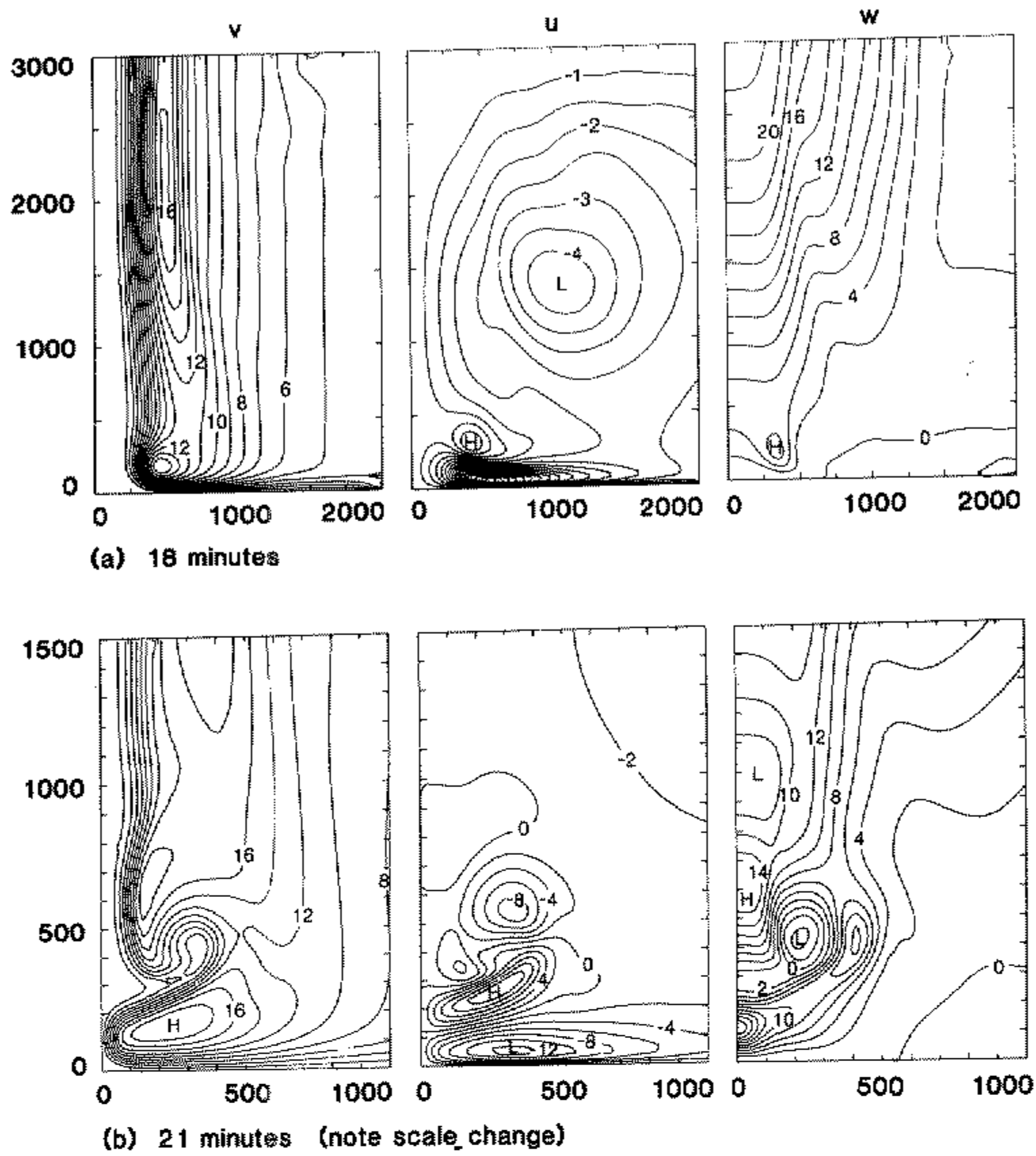
Figure 8. Transient meridional cross-sections of tangential, radial and vertical velocities for the case $V = 4\,\mathrm{m\,s^{-1}}$, $K = 10\,\mathrm{m^2\,s^{-1}}$ and a no-slip lower boundary: (a) at 18 minutes; and (b) at 21 minutes. (Note that (b) is plotted in the lower left-hand quadrant of the domain.)
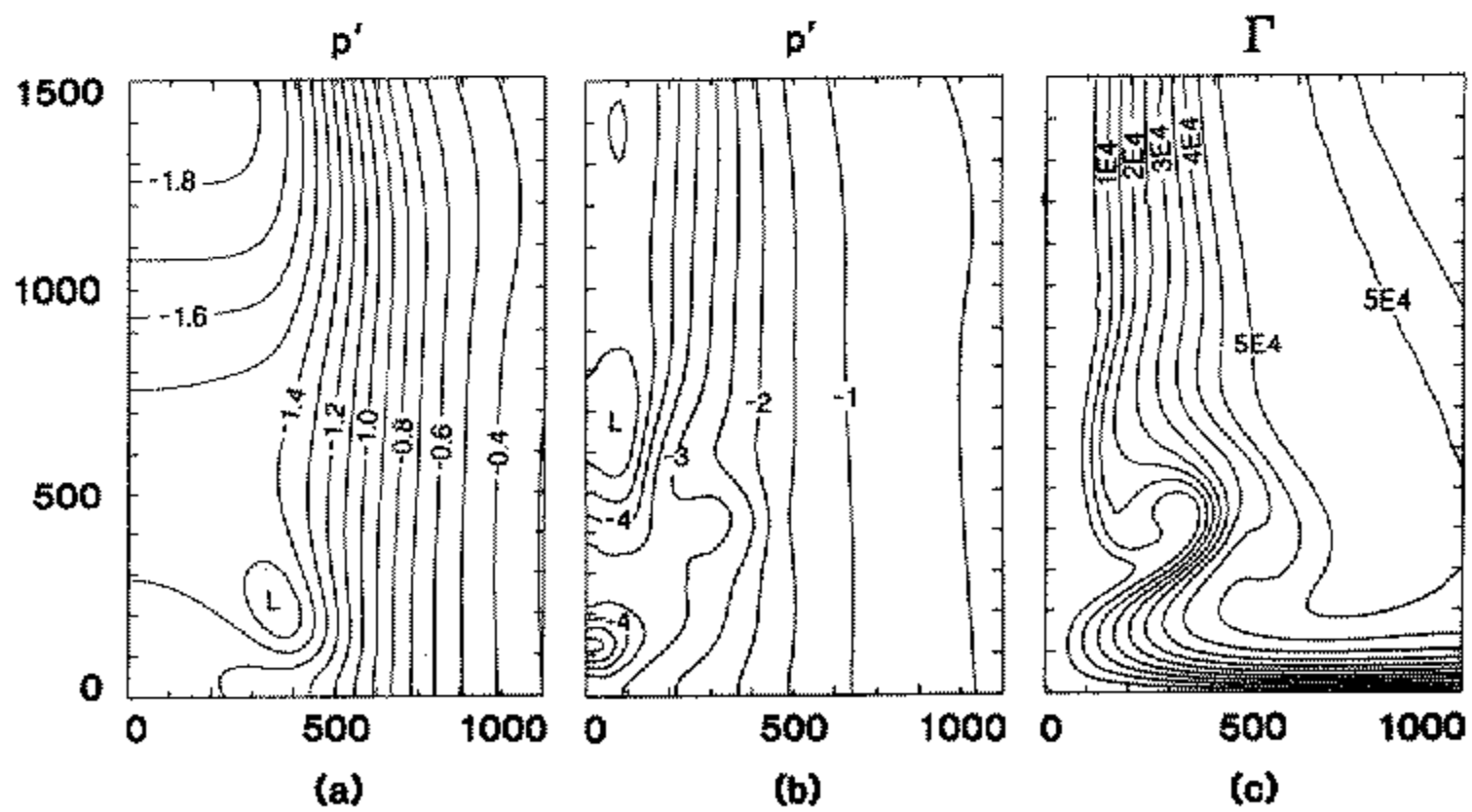

Figure 9. Meridional cross-sections (a) and (b) are the perturbation pressure fields at 18 minutes and 21 minutes respectively while (c) is the circulation field at 21 minutes. (Note that all diagrams are plotted in the lower left-hand quadrant of the domain.)

unable to describe the evolving flow pattern with a great degree of certainty due to the lack of a suitable turbulence closure scheme. If the integrations are continued, a series of centrifugal waves form along the axis. If the eddy diffusivity coefficient is raised to $20\,m^2\,s^{-1}$, the centrifugal wave breakdown is partially controlled. The inflow layer is broader, which is consistent with a terminal swirling boundary layer depth given by $\delta = R(K/\Gamma_o)^{1/2}$, where Γ_o is the outer conserved angular momentum. This relationship was proposed by Burggraf et al. (1971) and verified by Baker (1981) and Church and Snow (1984) using laboratory measurements.

Figure 10 shows the velocity components at 60 minutes for this experiment. The fields are quasi-steady in the sense that the breakdown feature is slowly propagating up the axis. The feature first appears at about 21 minutes at a height of 600 m and by 60 minutes has moved to 800 m. The details of the flow are similar to the previous case. An examination of the circulation field (not shown) reveals a very small region where the angular momentum surfaces fold but evidently there is enough diffusion in the present simulation to prevent the wave from breaking. In addition, it is clear that waves are not generated along the axis. The streamfunction (not shown) shows a toroidal vortex structure, with closed streamlines in the region where the stream surfaces expand. This ring vortex rotates relatively slowly around the axis in a region where the tangential velocity is reduced due to the sudden expansion of the vortex. The vertical flow through the ring vortex is only about $0.12\,m\,s^{-1}$ at 60 minutes.

If the eddy diffusivity coefficient is further increased to $30\,m^2\,s^{-1}$ and the experiment repeated the breakdown feature forms and is advected out of the domain leaving a steady one-cell vortex (Fig. 11). The maximum vertical velocity occurs near the base on the axis at a height of 500 m and is associated with a pressure minimum through the cyclostrophic balance across the vortex. The deceleration of the vertical flow above this level causes weak radial outflow and a subsequent expansion of the core. The maximum swirling winds are at low levels in contrast to the low-swirl velocity case. Evidently the radial inflow jet is able to inject rapidly rotating air close to the axis despite some frictional loss. Obviously in this parameter regime the vortices created by the concentration of vertical vorticity due to the primary and secondary sources of convergence are able to coexist in a stable configuration.

Figure 12 shows the time-section of axial vertical velocity. The breakdown feature is associated with retardation of axial flow and its position can clearly be traced along the axis. The speed of propagation is clearly much less than the speed of the updraught.

(iii) *Experiments with high imposed swirl velocity* ($S = 2$). Figure 13 shows the tangential, radial and vertical velocity meridional cross-sections at 15, 18 and 60 minutes respectively for the case $V = 10\,m\,s^{-1}$ and $K = 40\,m^2\,s^{-1}$. At 15 minutes the strong low-level rotation has produced flow separation on the axis. A downflow of $1.1\,m\,s^{-1}$ has developed at a height of 500 m. By 18 minutes a broad downdraught extends from 200 to 2700 m with a maximum downflow of $6.5\,m\,s^{-1}$ at the 500 m level. This transient feature resembles the downdraughts that were established in some of the free-slip experiments. Indeed, in both cases the origin for the downflow lies in the development of a low-level maximum in the swirling wind field. The downflow in the present experiment only lasts for about three minutes and eventually the flow pattern in Fig. 13(c) is established. There still exist two small regions of reversed axial flow; one at the 1000 m level, the other at 1500 m. Note that at upper levels, the axial flow is still considerably retarded with the maximum upflow above 500 m located some 250 m from the axis. The defect in the vertical velocity was also observed to occur in the free-slip experiments.
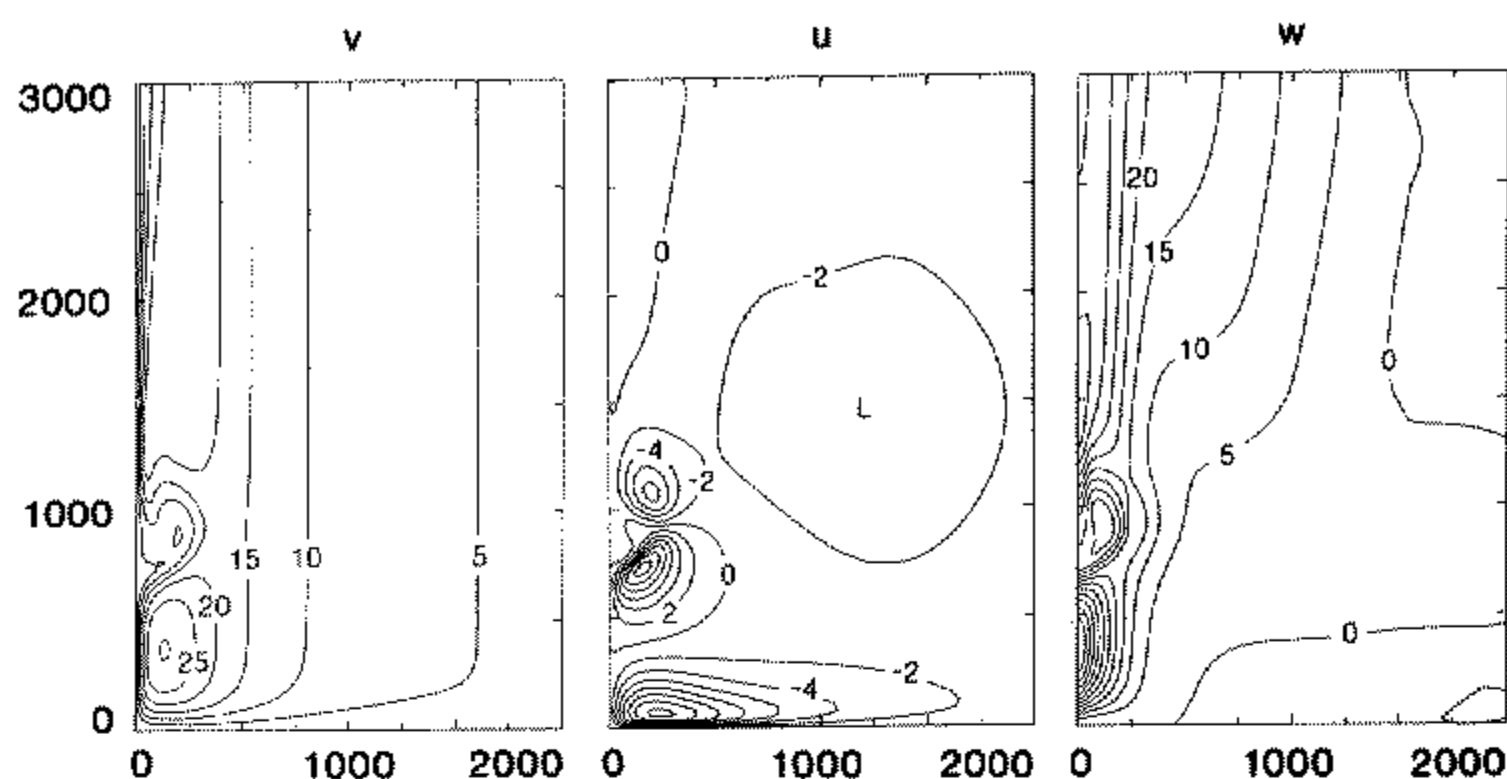
Figure 10. Steady-state meridional cross-sections of tangential, radial and vertical velocities for the case $V = 4\,\mathrm{m\,s^{-1}}$, $K = 20\,\mathrm{m^2 s^{-1}}$ and a no-slip lower boundary.
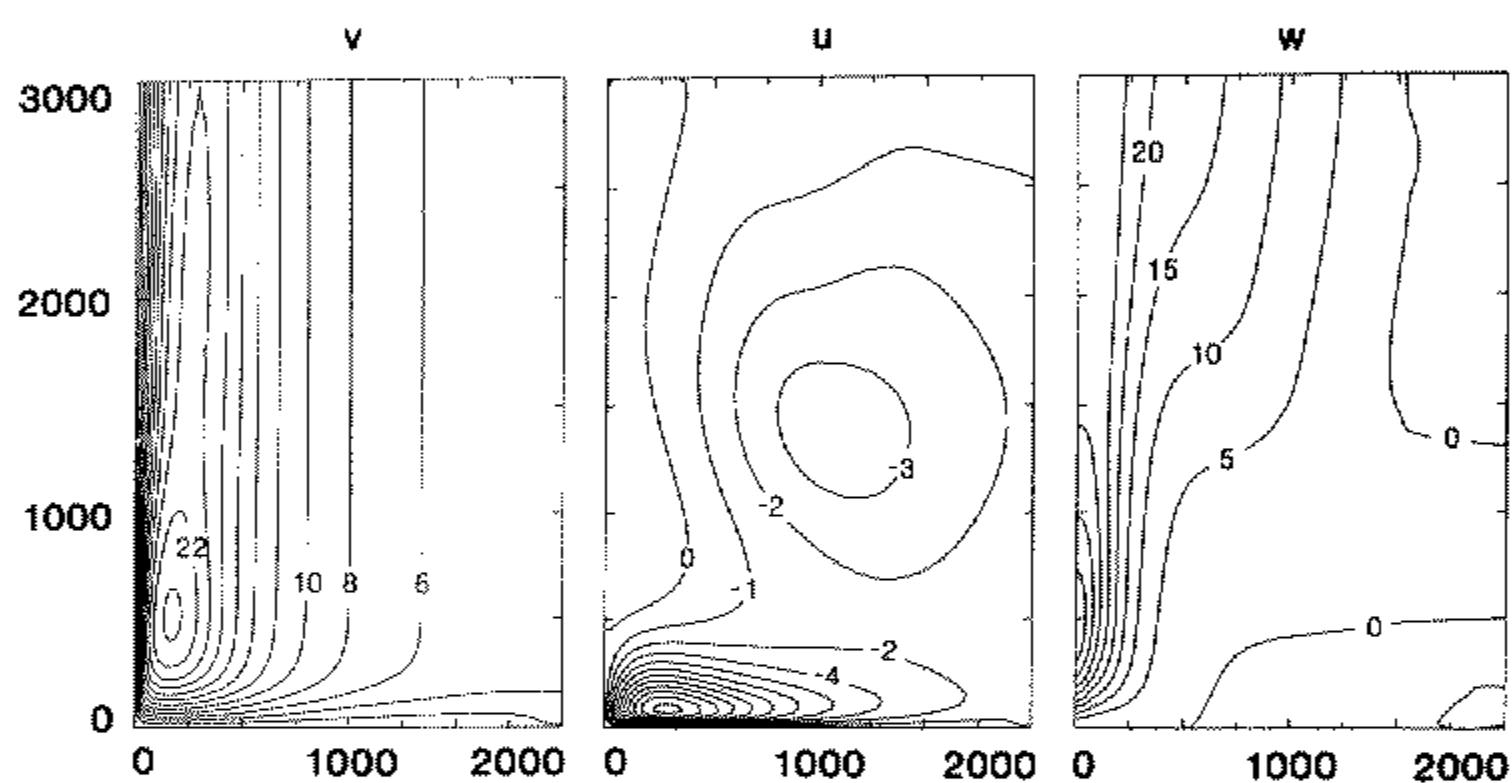

Figure 11. Steady-state meridional cross-sections of tangential, radial and vertical velocities for the case $V = 4\,\mathrm{m\,s^{-1}}$, $K = 30\,\mathrm{m^2 s^{-1}}$ and a no-slip lower boundary.
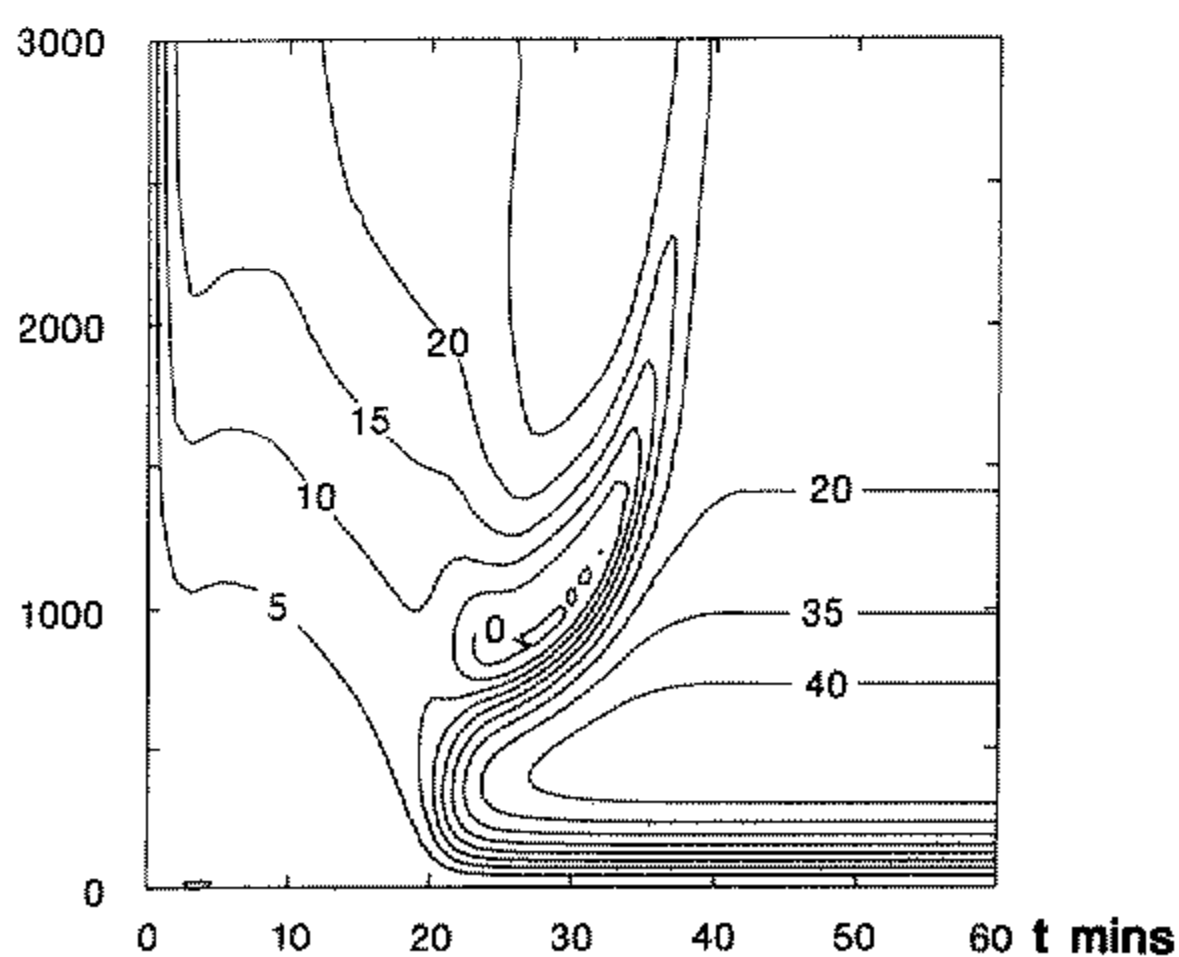

Figure 12. Time-section of axial vertical velocity for the case $V = 4\,\mathrm{m\,s^{-1}}$, $K = 30\,\mathrm{m^2 s^{-1}}$ and a no-slip lower boundary.
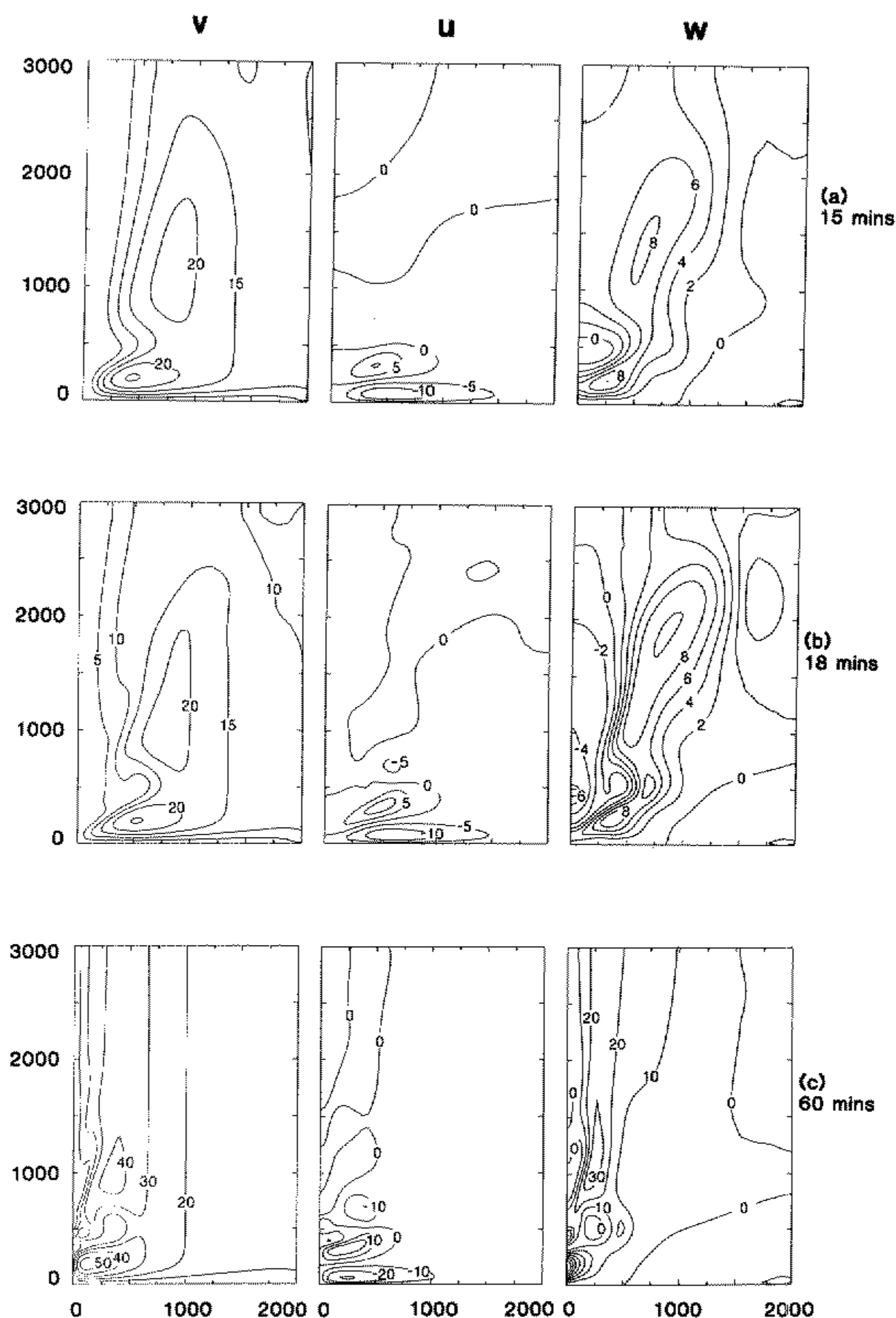
Figure 13. Meridional cross-sections of tangential, radial and vertical velocities for the case $V = 10\,\mathrm{m\,s^{-1}}$, $K = 40\,\mathrm{m^2\,s^{-1}}$ and a no-slip lower boundary at various times as indicated.

The flow near the corner region strongly resembles the flow structure obtained in the moderate swirl velocity case $V = 4\,\mathrm{m\,s^{-1}}$, $K = 20\,\mathrm{m^2\,s^{-1}}$ with a toroidal vortex situated 400 m from the axis at the 500 m level. The fields at 60 minutes are quasi-steady and a history of the maximum vertical and tangential velocity reveals a gradual increase of flow variables with time. The maximum inflow speed associated with the radial jet at 60 minutes is $31\,\mathrm{m\,s^{-1}}$ with a corresponding axial updraught of $79\,\mathrm{m\,s^{-1}}$. The swirling winds are very strong at low levels with a maximum speed of $55\,\mathrm{m\,s^{-1}}$. This is considerably higher than the maximum swirl velocity obtained in the corresponding free-slip experiment (Fig. 5(c)), which attained a speed of $41\,\mathrm{m\,s^{-1}}$.

4. DISCUSSION AND CONCLUSIONS

This paper demonstrates the importance of the lower boundary condition and the eddy diffusivity coefficient in influencing the dynamics of the evolving vortex and, in particular, the evolution of vortex breakdown. The no-slip condition produces a radial inflow jet due to the breakdown of cyclostrophic wind balance near the ground. This secondary source of convergence of rotating air can play an important role in determining such important aspects as vortex strength, the stability of the flow and the type of vortex structure (i.e. one- or two-cell). For weak applied swirl velocities (about $1 \mathrm{m s}^{-1}$ in the current experimental configuration), the no-slip condition produces sufficient frictional loss near the lower boundary to create a vortex with maximum swirl velocity aloft despite the enhanced inflow at low levels (this inflow occurred in all the simulations using various values of the diffusivity coefficient). Cyclostrophy then implies that air parcels should accelerate along much more of the axis. The no-slip condition will always favour a one-cell structure as a consequence of the axial jet erupting from the corner region as an extension of the swirling boundary layer. At higher applied swirl velocities (about $4 \mathrm{m s}^{-1}$ or more in the current work), the radial jet transports rapidly rotating air close to the axis so that the maximum swirling velocities in the domain occur near the corner region. The stability of the ensuing flow depends largely on the amount of eddy mixing, which, as stated, is subject to considerable uncertainty in rapidly rotating atmospheric flows. Using a diffusivity coefficient of $10 \mathrm{m}^2 \mathrm{s}^{-1}$ resulted in a large amplitude centrifugal wave forming as the inflow jet developed inertial overshoot. Subsequently, this wave broke violently near the axis. The higher diffusivity coefficient of $20 \mathrm{m}^2 \mathrm{s}^{-1}$ produced a quasi-steady toroidal vortex within the region where the streamlines expanded similar to Harlow and Stein (1974). The breakdown feature was advected out of the domain when the diffusivity coefficient was increased to $30 \mathrm{m}^2 \mathrm{s}^{-1}$ leaving a steady one-cell vortex with a retardation in vertical velocity and associated radial outflow above the level of maximum tangential winds. The no-slip condition can lead to the development of internal vortices with associated axial downdraughts (a large transient downdraught developed in the high-swirl velocity experiment at 18 minutes). It is conjectured that the no-slip case, with large swirl velocity at low levels, leads to a competition between the axial end-wall updraught and retarded vertical flow aloft. Vortex breakdown occurs when these two flow features interact catastrophically (Rotunno 1980). In the present experimental configuration, with the applied vertical body force, the one-cell structure is always favoured if the flow recovers from breakdown.

In order to highlight the controlling influence of the radial inflow jet, free-slip experiments were performed using the same values of applied swirl velocity and diffusivity coefficient as were adopted in the no-slip study. In all of the experiments conducted, no dynamic instabilities associated with the large-scale flow were observed to occur. The type of vortex that develops is largely controlled by the amount of turbulent mixing with large values of the diffusivity coefficient inhibiting the development of a steady two-cell vortex structure due to the increase in mixing of vertical momentum across the core. In these free-slip experiments, a reduction in the axial velocity occurred in all simulations with the maximum vertical velocity in the domain located off the axis. Mixing of azimuthal momentum near the axis resulted in the maximum swirling wind occurring at low levels in all cases. A comparison of the maximum tangential, radial and vertical velocities is given in Table 1. At low applied swirl velocities, the free-slip vortex is stronger than the equivalent no-slip case whilst the opposite is true at higher swirl velocities. This reinforces the notion that the radial inflow jet plays a very important role in determining the strength and structure of the vortex, particularly at higher applied swirl velocities. The strength

TABLE 1.   MAXIMUM VALUE OF FLOW PARAMETERS IN THE DOMAIN WITH FREE-SLIP AND NO-SLIP CONDITIONS AT THE SURFACE WITH VARIOUS VALUES OF APPLIED SWIRL VELOCITY AND DIFFUSIVITY COEFFICIENT AS INDICATED

V	K	No-slip			Free-slip		
		v_{max}	u_{max}	w_{max}	v_{max}	u_{max}	w_{max}
1	4	10	3·6	24	23	3·9	19
4	20	30	15	55	31	3·8	19
4	40	20	9·0	35	26	3·8	18
10	40	55	31	79	42	3·5	17

All velocities are in m s^{-1} and diffusivity coefficients in m^{2}s^{-1}.

of the free-slip vortex is largely controlled by the primary source of convergence of ambient swirling air, in this case, the applied body force.

The present work demonstrates the importance of the proper representation of subgrid-scale processes in modelling rapidly rotating atmospheric flows. In this study, the value of the constant eddy diffusivity coefficient was chosen on the basis of preventing strong shear layers from forming in the boundary layer and vortex core. If the gradients of the flow variables become too large, then the numerical finite-difference procedure suffers from a rapid increase in local truncation errors and the computational procedure eventually fails. In reality, strong shear layers might correspond to the development of turbulent subgrid-scale eddies unresolvable on the scale of the present grid and such effects would inevitably decrease the magnitude of the shear, particularly in regions which are not either stably stratified or centrifugally stable. This concept is consistent with Turner's (1966) hypothesis of self-regulating turbulence in rapidly rotating atmospheric vortices. For the free-slip experiments, the magnitude of the eddy diffusivity coefficient determined whether the flow had a one- or two-cell structure. For the no-slip experiment it had a controlling influence on many flow features including vortex breakdown and the magnitude and position of the maximum in the swirling winds. From the above we may infer that if the diffusivity coefficient is large for a given applied swirl velocity, the maximum winds will occur near the top of the domain due to the frictional loss near the lower surface. In the other extreme, if the diffusivity coefficient is small in relation to the applied swirl velocity, catastrophic vortex breakdown may occur due to the breaking of a large amplitude centrifugal wave near the corner region as the inflow jet develops inertial overshoot. Between these two extremes, steady one-cell vortices develop with maximum swirl velocity at low levels and there is a possibility of quasi-steady breakdown features such as a toroidal vortex located a short distance above the lower boundary. Due to the extreme sensitivity of the flow to the value of the eddy diffusivity coefficient, any attempt to simulate actual atmospheric vortices using a model which incorporates self-regulating subgrid turbulence closure should include a thorough sensitivity test of the parameters assumed within the closure approximation.

Finally a note on the relevance of the study to atmospheric vortices. Due to the infrequent observations of bulge-like features in tornadoes, we may conclude that the turbulence levels may actually be quite high. In the case of waterspouts, it is more likely that the updraught concentrates a rather weak supply of ambient vorticity. Observational studies of tornadoes using photogrammetric analysis (e.g. see Hoecker 1960 and Golden and Purcell 1978) indicate that the strongest swirling and rising motions occur close to the ground. Moreover, the existence of an intense inflow jet (although somewhat

asymmetrical) has also been established. These results resemble the simulations performed with no-slip conditions using a moderate to high imposed swirl velocity. Although some observational studies have revealed subsidence in the immediate vicinity of the funnel cloud (e.g. see Hoecker 1959; Golden and Purcell 1978; Fujita 1975, 1976; Forbes 1979), it is likely that this is associated with storm-scale downdraughts rather than a breakdown feature like a toroidal vortex.

This work emphasizes the importance of frictional processes in determining vortex flow characteristics, including the intensity of the winds. To date there have been no estimates made of turbulence levels in rapidly rotating atmospheric flows. Until data become available, we can only improve the current axisymmetric model by adopting the conventional turbulence parametrizations that have been widely used in studies of other atmospheric phenomena. Such an investigation will form the basis of future research.

APPENDIX A

Nomenclature

c_p	specific heat of dry air at constant pressure
$\mathcal{D}$	second-order diffusion operator
F	prescribed body force
g	acceleration due to gravity
H	model domain height (3000 m)
K	constant eddy diffusivity coefficient
r	stretched radial coordinate
R	model domain radius (2000 m)
R_e	Reynolds' number $= UR/K$
R_i	Richardson number (see Eq. (3.5))
S	swirl ratio $= V/\bar{w}$
t	time
u	radial velocity
U	typical inflow velocity at the radial boundary
v	azimuthal (tangential or swirl) velocity
V	imposed tangential velocity at the radial boundary
w	vertical velocity
$\bar{w}$	average vertical velocity through the top boundary
x	non-stretched radial coordinate
Δx	constant non-stretched radial grid spacing
y	non-stretched vertical coordinate
Δy	constant non-stretched vertical grid spacing
z	stretched vertical coordinate
α, β	grid stretching parameters
Γ	circulation ($2\pi r v$)
Γ_o	outer flow circulation
δ	boundary layer thickness

η azimuthal vorticity
θ potential temperature
θ_a potential temperature deviation from ambient state
$\Delta\theta$ maximum temperature deviation in the body forcing
κ adiabatic constant for dry air $= 0\cdot286$
κ_H, κ_Z horizontal and vertical eddy diffusivity coefficients (both equivalent to K in this study)
ν_H, ν_Z horizontal and vertical eddy viscosity coefficients (both equivalent to K in this study)
π Exner function ($= (p/1000)^\kappa$, p is pressure in mb)
ρ_a ambient density
ϕ azimuthal angle
ψ streamfunction

subscript 'a'   the ambient value of a quantity at the same height
prime   the deviation of a quantity from its ambient value at the same height

$D/Dt = \partial/\partial t + u\,\partial/\partial r + w\,\partial/\partial z$,   the total derivative

APPENDIX B

Basic equations and boundary conditions

As in Howells and Smith (1983), the radial and vertical momentum equations, namely

$$\frac{Du}{Dt} - \frac{v^2}{r} = -c_p \frac{\partial}{\partial r}(\theta_a \pi') + \mathcal{D}_u$$

and

$$\frac{Dw}{Dt} = -c_p \frac{\partial}{\partial z}(\theta_a \pi') + g\left(\frac{\theta'}{\theta_a}\right) + F + \mathcal{D}_w$$

are cross-differentiated to form a prognostic equation for azimuthal vorticity, i.e.

$$\frac{D\eta}{Dt} = \left(\frac{2w}{\rho_a}\frac{\partial \rho_a}{\partial z} + \frac{u}{r}\right)\left(\eta - u\frac{\partial \rho_a}{\partial z}\right) + uw\frac{\partial^2 \rho_a}{\partial z^2} + \frac{1}{r}\frac{\partial}{\partial z}(\rho_a v^2) - $$

$$- c_p \theta_a \frac{\partial \pi'}{\partial r}\frac{\partial \rho_a}{\partial z} - \rho_a g \frac{\partial}{\partial r}\left(\frac{\theta'}{\theta_a}\right) - \rho_a \frac{\partial F}{\partial r} + \mathcal{D}_\eta.$$

Equations for the conservation of angular momentum and potential temperature are respectively

$$Dv/Dt + uv/r = \mathcal{D}_v \quad \text{and} \quad D\theta/Dt = \mathcal{D}_\theta.$$

A streamfunction ψ is introduced to ensure that the equation of continuity of mass is satisfied. The diagnostic equation for ψ is

$$r\eta = r\frac{\partial}{\partial r}\left(\frac{1}{r}\frac{\partial \psi}{\partial r}\right) + \frac{\partial^2 \psi}{\partial z^2}$$

and note that $\rho_a r u = \partial \psi/\partial z$, $\rho_a r w = -\partial \psi/\partial r$. The diffusion terms in the above equations are expressed as

$$\mathscr{D}_\eta = \nu_H \frac{\partial}{\partial r}\left(\frac{1}{r}\frac{\partial(r\eta)}{\partial r}\right) + \nu_Z \frac{\partial}{\partial z}\left[\rho_a\frac{\partial}{\partial z}\left(\frac{\eta}{\rho_a}\right) - \rho_a u\frac{\partial}{\partial z}\left(\frac{1}{\rho_a}\frac{\partial\rho_a}{\partial z}\right)\right]$$

$$\mathscr{D}_v = \nu_H \frac{\partial}{\partial r}\left(\frac{1}{r}\frac{\partial(rv)}{\partial r}\right) + \nu_Z \frac{1}{\rho_a}\frac{\partial}{\partial z}\left(\rho_a\frac{\partial v}{\partial z}\right)$$

$$\mathscr{D}_\theta = \kappa_H \frac{1}{r}\frac{\partial}{\partial r}\left(r\frac{\partial\theta}{\partial r}\right) + \kappa_Z \frac{1}{\rho_a}\frac{\partial}{\partial z}\left(\rho_a\frac{\partial\theta}{\partial z}\right).$$

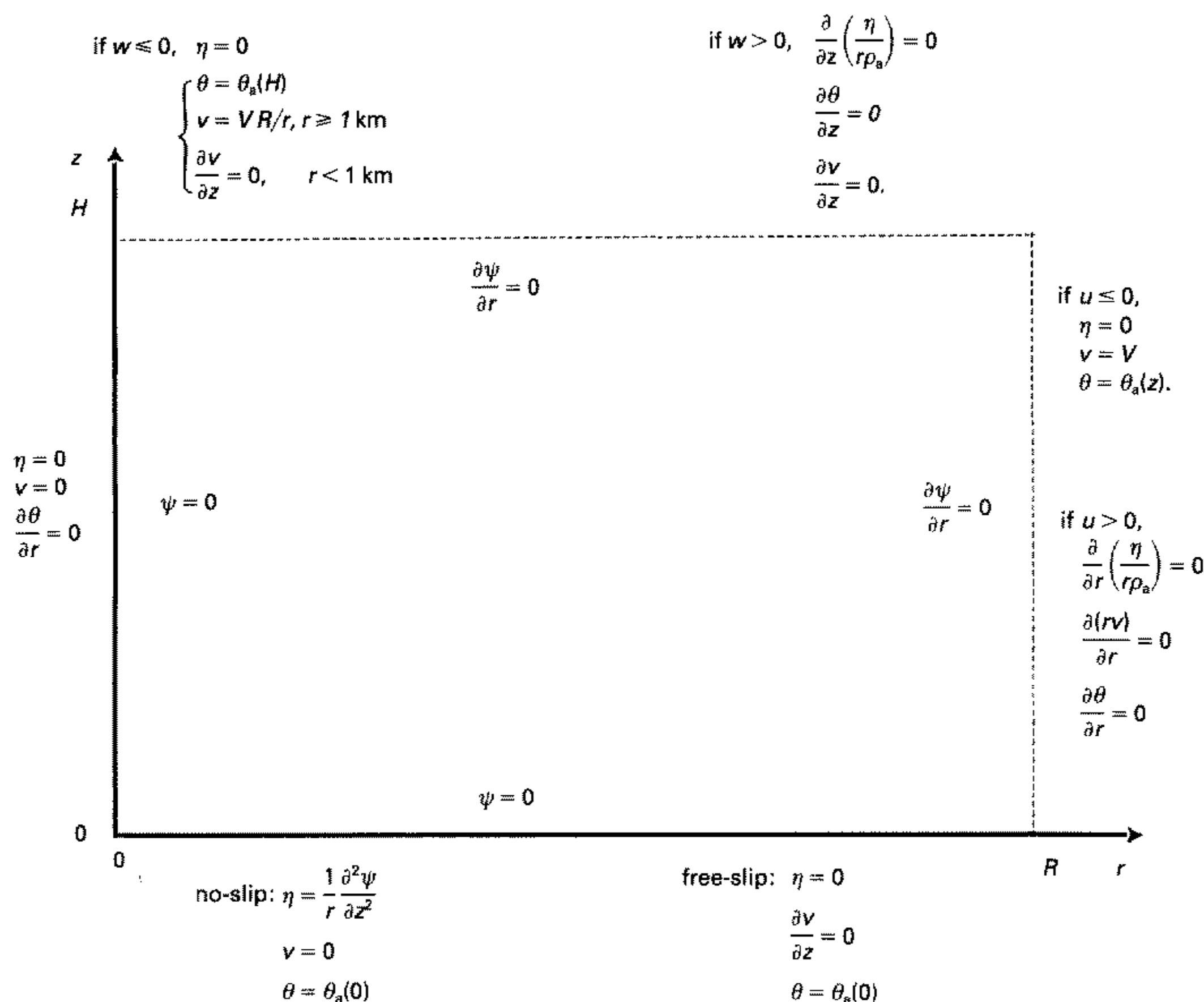Boundary conditions for the model are summarized in Fig. B1.

Figure B1. Boundary conditions.

REFERENCES

Anthes, R. A.	1970	Numerical experiments with a two-dimensional horizontal variable grid. *Mon. Weather Rev.*, **98**, 810–822
Baker, G. L.	1981	'Boundary layers in laminar vortex flows'. Ph.D. thesis, Purdue Univ. Available from Univ. Microfilms Inc., Ann. Arbor, MI, order number DA 8210153
Benjamin, T B.	1962	Theory of vortex breakdown phenomena. *J. Fluid Mech.*, **14**, 593–629
	1967	Some developments in the theory of vortex breakdown, *ibid.*, **28**, 65–84
Bode, L, Leslie, L. M. and Smith R. K.	1975	A numerical study of boundary effects on concentrated vortices with application to tornadoes and waterspouts. *Q. J. R. Meteorol. Soc.*, **101**, 313–324

Burggraf, O. R., Stewartson K. and Belcher, R.   1971   Boundary layer induced by a potential vortex. *Phys. Fluids*, **14**, 1821-1833

Carrier, G. F.   1971   Swirling flow boundary layers. *J. Fluid Mech.*, **49**, 133-144

Church, C. R. and Snow, J. T.   1985   Measurements of axial pressure in tornado-like vortices. *J. Atmos. Sci.*, **42**, 576-582

Church, C. R., Snow, J. T. and Agee, E. M.   1979   Tornado vortex simulations at Purdue University. *Bull. Am. Meteorol. Soc.*, **60**, 900-908

Drazin, P. G. and Reid, W. R.   1982   *Hydrodynamic stability*. Cambridge Univ. Press

Forbes, G. S.   1979   'Observations of relationships between tornado structure, underlying surface, and tornado appearance'. Pp. 351-356 in *Preprints, 11th Conf. on Severe Local Storms*. 2-5 Oct. 1979. Kansas City. American Meteorological Society

Fujita, T. T.   1975   'New evidence from April 3-4, 1974 tornadoes'. Pp. 248-255 in *Preprints, 9th Conf. on Severe Local Storms*. 21-23 Oct. 1975. Norman. American Meteorological Society

    1976   'History of suction vortices'. Pp. 78-80 in *Proc. Symp. on Tornadoes: Assessment of knowledge and implications for man*. Texas Tech. Univ., Lubbock

Gartshore, I. S.   1962   'Recent work in swirling incompressible flow'. NRC Canada, Aero. Rep. LR-343

Golden, J. W. and Purcell, D.   1978   Airflow characteristics around the Union City tornado. *Mon. Weather Rev.*, **106**, 22-28

Hall, M. G.   1967   'A new approach to vortex breakdown'. Pp. 319-340 in *Proc. 1967 Heat Transfer and Fluid Mechanics Institute*. Stanford Univ. Press

    1972   Vortex breakdown. *Ann. Rev. Fluid Mech.*, **4**, 195-218

Harlow, F. H. and Stein, L. R.   1974   Structural analysis of tornado-like vortices. *J. Atmos. Sci.*, **31**, 2081-2098

Hoecker, W. H., Jr.   1959   History and measurements of the two major Scottsbluff tornadoes of 27 June 1955. *Bull. Am. Meteorol. Soc.*, **40**, 117-133

    1960   Wind speed and air flow patterns in the Dallas tornado of 2 April 1957. *Mon. Weather Rev.*, **88**, 1167-1180

Howard, L. N. and Gupta, A. S.   1962   On the hydrodynamic and hydromagnetic stability of swirling flows. *J. Fluid Mech.*, **14**, 463-476

Howells, P. and Smith, R. K.   1983   Numerical simulations of tornado-like vortices. Part I: Vortex evolution. *Geophys. Astrophys. Fluid Dyn.*, **27**, 253-284

Lewellen, W. S. and Sheng, K. P.   1980   'Modeling tornado dynamics'. Final report to U.S. Nuclear Regulatory Commission (NTIS NUGREG/CR-1585)

Lewellen, W. S. and Teske, M. E.   1977   'Turbulent transport model of low level winds in a tornado'. Pp. 291-298 in *Preprints 10th Conf. on Severe Local Storms*. 18-21 Oct. 1977. Omaha. American Meteorological Society

Ogura, Y. and Phillips, N. A.   1962   A scale analysis of deep and shallow convection in the atmosphere. *J. Atmos. Sci.*, **19**, 173-179

Rayleigh, Lord   1916   On the dynamics of revolving fluids. *Proc. R. Soc. London*, **A93**, 148-154

Rotunno, R.   1977   Numerical simulation of a laboratory vortex. *J. Atmos. Sci.*, **34**, 1942-1956

    1979   A study in tornado-like vortex dynamics. *ibid.*, **36**, 140-155

    1980   Vorticity dynamics of a convective swirling boundary layer. *J. Fluid Mech.*, **97**, 623-640

Smith, R. K. and Howells, P.   1983   Numerical simulations of tornado-like vortices. Part II: Two-cell vortices. *Geophys. Astrophys. Fluid Dyn.*, **27**, 285-298

Smith, R. K. and Leslie, L. M.   1976   Thermally driven vortices: A numerical study with application to dust devil dynamics. *Q. J. R. Meteorol. Soc.*, **102**, 791-804

Turner, J. S.   1966   The constraints imposed on tornado-like vortices by the top and bottom boundary conditions. *J. Fluid Mech.*, **25**, 377-400

Ward, N. B.   1972   The exploration of certain features of tornado dynamics using a laboratory model. *J. Atmos. Sci.*, **29**, 1194-1204

Wilson, T. and Rotunno, W. R.   WR 1986   A numerical simulation of a laminar end-wall vortex and boundary layer. *Phys. Fluids*, **29**, 3993-4005